**Journal of Engineering Mechanics and Machinery (2026)**
**Clausius Scientific Press, Canada**

**DOI: 10.23977/jemm.2026.110111**
**ISSN 2371-9133 Vol. 11 Num. 1**

# *Dynamic Response Analysis of Sieve Screening under Complex Working Conditions*

**Jiang Zhihong**[1,a,*], **Luo Zhuqing**[2,b]

*[1]School of Mechanical and Electrical Engineering, Jiangxi University of Science and Technology, Ganzhou, Jiangxi Province, 341000, China*
*[2]Key Laboratory of Granular Technology, Ganzhou, Jiangxi Province, 341000, China*
*[a]3055279800@qq.com, [b]6720230533@email.jxust.edu.cn*

***Keywords:*** Spring Damage Amount; Complex Working Conditions, Dynamic Modeling, Numerical Simulation, Screening Surface State

***Abstract:*** To explore the influence of silo load and material distribution on the motion characteristics of partition screens, a four-degree-of-freedom dynamic model was established via the Lagrange method. The model was solved for different spring damage degrees and load conditions using the New-Mark β method. Results indicate that under complex operating conditions involving silo mass and uneven material distribution, the screen surface exhibits enhanced instability—with the feed end showing downward tilting and an increased swing angle. The amplitudes in the z and y directions increase with the degree of spring damage, whereas the amplitudes in the θ and φ directions and the location of spring damage are associated with the severity of spring damage. Under varying load and spring damage conditions, the displacement difference between springs increases linearly with load magnitude. At the same end of the screen, the inter-spring displacement difference ranges from 32% to 93%. Under the same load, diagonal spring damage leads to the maximum inter-spring displacement difference (221%), inducing severe screen vibration.

## 1. Introduction

Traditional early-stage dynamics research primarily adopted simplified models such as single-degree-of-freedom (SDOF) and two-degree-of-freedom (2DOF) systems. While these models offer the advantages of simplified modeling and low computational cost—enabling the rapid satisfaction of basic design requirements—they have notable limitations [1-4]. Specifically, they struggle to accurately characterize the spatially coupled motion of screen bodies, material impact loads, and the dynamic properties of novel vibration isolation components [4-7]. Furthermore, they often neglect the inertial effects of ore and the actual forces acting on the screen surface, rendering the equipment prone to resonance and unstable vibrations [8-9].

To address these drawbacks, scholars have proposed various optimization schemes and models tailored to specific requirements in recent years, each with distinct merits and limitations. Constructed via the Lagrange method and solved using the Runge-Kutta method, the spatial six-degree-of-freedom (6DOF) model accurately captures the coupled motion behaviors of screens, with model-test deviations generally within 10%. Nevertheless, this model involves complex construction and demands highly accurate parameter inputs [10-11]. The small-damping three-degree-of-freedom (3DOF) model, specifically designed for specialized equipment such as double-layer vibrating retarding screens, effectively mitigates vibration instability, achieving prediction deviations of less than 10% for both amplitude and natural frequency. Nonetheless, its limited versatility hinders its application to other types of vibrating screens [12-13]. The dynamic model integrated with auxiliary chamber air springs suppresses resonance effectively through variable stiffness and high damping properties, yielding a simulation-experimental amplitude deviation of only 1% while enabling precise control of screening parameters. However, its derivation necessitates the integration of thermodynamics and fluid mechanics theories, posing considerable modeling challenges [13-14]. The discrete element method (DEM)-coupled simulation overcomes the simplifying assumptions of traditional material models by accurately calculating the actual forces exerted by ore on the screen surface and simulating practical problems such as screen hole clogging, showing strong consistency with industrial applications. Nevertheless, it entails substantial computational demands, stringent hardware requirements, and complex modeling processes for non-spherical particles [15-16].

Notably, the aforementioned simulation experiments and dynamic equations are based on the motion characteristics of the vibrating screen surface (e.g., screen surface amplitude and trajectory), conducted under the assumption of neglecting the material mass distribution inside the screen box. However, the screen surface motion characteristics under different loading conditions—such as material displacement and initial compression from the material bin—have not been analyzed or addressed.

In response to the feeding difficulty encountered by vibrating screens after long-term operation, this paper establishes a four-degree-of-freedom (4DOF) dynamic model incorporating spring position distribution, considering the influences of factors such as material distribution, bin load, and the number of damaged springs. It investigates the effects of the number of damaged springs in the bar screen and material distribution on the screen surface amplitude response.

## 2. Mathematical Model

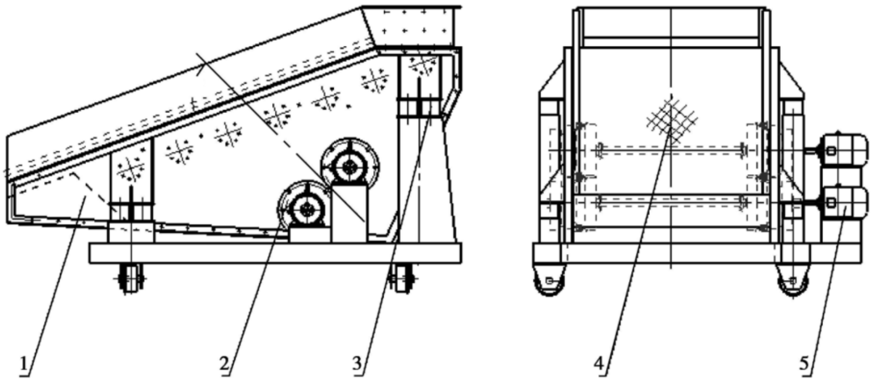

1—frame; 2—vibration sources; 3—damping device; 4—sieve tray; 5—electromotor

Fig.1 Three-dimensional schematic diagram of the partition screen

As illustrated in Figure 1, the partition screen assembly comprises a screen frame, sieve plates, a spring-based vibration damping system, an excitation source, a material hopper, and auxiliary components. The physical model is simplified to focus on the sieve surface, where the material hopper and excitation system primarily exert vibratory forces along the vertical and feed directions. Springs are distributed around the periphery of the sieve surface. The load from the material hopper acts on the feed end of the partition screen and is modeled as a uniformly distributed load. The moment generated by the mass of the hopper exerts a force on the sieve surface. Moreover, due to the non-uniform distribution of material across the sieve surface, localized moments are induced on specific sides of the sieve.

The screening plane is simplified as a rigid-plane body, and a spatial Cartesian coordinate system is established (see Figure 2). The origin of the coordinate system is situated at the center of mass of the rigid body, where the z-axis is perpendicular to the screening plane, and the x-axis and y-axis lie within the plane. Specifically, the x-axis is aligned with the axial direction of the rigid body (perpendicular to the side plates of the screen bars), while the y-axis corresponds to the radial direction (i.e., the line connecting the feed end and discharge end of the screen bars). The excitation force is a periodic harmonic vibration that acts perpendicular to the x-axis and is confined to the yz-plane. Under this excitation, the rigid-plane body of the vibrating screen primarily undergoes translational motions along the y-axis and z-axis, as well as rotations about the x-axis and y-axis. Thus, this model focuses on four degrees of freedom: translational displacements along the y-axis (denoted as y) and z-axis (denoted as z), and angular displacements about the x-axis (denoted as θ) and y-axis (denoted as φ).

The four elastic supporting springs ($k_1$、$k_2$、$k_3$ $and$ $k_4$) are decomposed into mutually perpendicular components in the y-direction and z-direction, which are denoted as $k_{yi}$ and $k_{zi}(i = 1、2、3、4)$ respectively. The rigid body has an axial length of 2$a$, a radial length of 2$b$, a mass of m, and mass moments of inertia about the x-axis and y-axis of $J_x$ $and$ $J_y$ respectively. The excitation force rotates about the x-axis within the yz-plane, with an amplitude of $f$ and an angular velocity of $\omega$. The gravitational force $G$ of the material hopper acts with a moment arm $e$, thereby generating a torque $Ge$ on the screen surface. Additionally, a torque $M_e$ is induced by the displacement of the material.

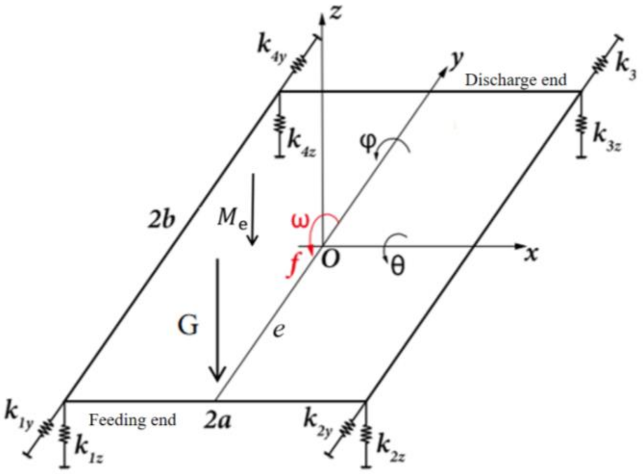

Fig 2. Physical model of the partition screen

(1) System kinetic energy$E_k$:

$$E_k=\frac{1}{2}J_x\dot{\theta}^2+\frac{1}{2}J_y\dot{\varphi}^2+\frac{1}{2}m\dot{z}^2+\frac{1}{2}m\dot{y}^2 \qquad (1)$$

In this formula, $J_x$ represents the system's moment of inertia in the $x$ direction, $J_y$ denotes the moment of inertia in the $y$ direction, $\theta$ and $\varphi$ are the angular velocities in the $\theta$ and $\varphi$ directions respectively, $m$ stands for the system's mass, $z$ and $y$ are the velocities in the $z$ and $y$ directions respectively.

(2) System potential energy $E_p$:

$$E_p = \sum_{i=1}^{16} \frac{1}{2} k_{iz} \Delta Z_i^2 + \sum_{i=1}^{16} \frac{1}{2} k_{iy} \Delta Y_i^2 \quad (2)$$

Here, $k_{iz}$ denotes the stiffness of the $i$-th spring in the z direction, $k_{iy}$ represents its stiffness in the $y$ direction, while $\Delta Z_i$ and $\Delta Y_i$ indicate the deformation amounts in the $z$ and $y$ directions respectively. The spatial coordinates of the spring are$(x_1, y_1), (x_2, y_2), (x_3, y_3), (x_4, y_4)$

Spring deformation:

$$\Delta Z_i = z + y_i \theta + x_i \varphi$$

$$\Delta Y_i = y + y_i \theta$$

Substituting (1) and (2) into the Lagrange equation, we obtain the system's vibration equation (3).

$$M\ddot{X} + KX = F \quad (3)$$

Here, $\ddot{x}$ represents the system's inertia vector $\ddot{X}=(\ddot{y}\ \ddot{z}\ \ddot{\theta}\ \ddot{\varphi})^T$ ,while $F$ represents the displacement vector $X=(y\ z\ \theta\ \varphi)^T$ . The generalized force vector F is defined as $F = (f sin\omega t\ \ f cos\omega t\ \ Ge\ \ M_e)^T$. The excitation motor acts in the $y$-$z$ plane, decomposing the excitation force $f$ into $y$-direction components $f sin\omega t$ and $z$-direction components $f cos\omega t$ The material hopper exerts a torque $Ge$ on the sieve surface, and the torque generated by material displacement is $M_e$.

M The system quality matrix:

$$M = \begin{bmatrix} m & 0 & 0 & 0 \\ 0 & m & 0 & 0 \\ 0 & 0 & J_x & 0 \\ 0 & 0 & 0 & J_y \end{bmatrix}$$

$K$ The system stiffness matrix:

$$K = \begin{bmatrix} k_{11} & k_{12} & k_{13} & k_{14} \\ k_{21} & k_{22} & k_{23} & k_{24} \\ k_{31} & k_{32} & k_{33} & k_{34} \\ k_{41} & k_{42} & k_{43} & k_{44} \end{bmatrix}$$

Inside

$$k_{11} = k_{1y} + k_{2y} + k_{3y} + k_{4y}$$

$$k_{12} = k_{21} = 0$$

$$k_{13} = k_{31} = -(k_{1y}y_1 + k_{2y}y_2 + k_{3y}y_3 + k_{4y}y_4)$$

$$k_{14} = k_{41} = 0$$

$$k_{22} = k_{1z} + k_{2z} + k_{3z} + k_{4z}$$

$$k_{23} = k_{32} = k_{1z}x_1 + k_{2z}x_2 + k_{3z}x_3 + k_{4z}x_4$$

$$k_{24} = k_{42} = k_{1z}y_1 + k_{2z}y_2 + k_{3z}y_3 + k_{4z}y_4$$

$$k_{33} = k_{1y}y_1^2 + k_{2y}y_2^2 + k_{3y}y_3^2 + k_{4y}y_4^2 + k_{1z}x_1^2 + k_{2z}x_2^2 + k_{3z}x_3^2 + k_{4z}x_4^2$$

$$k_{34}=k_{43}=k_{1z}x_1y_1+k_{2z}x_2y_2+k_{3z}x_3y_3+k_{4z}x_4y_4$$

$$k_{44}=k_{1y}y_1^2+k_{2y}y_2^2+k_{3y}y_3^2+k_{4y}y_4^2$$

## 3. Parameters and Scheme Design

The parameters (as shown in Table 1) are sourced from the YVF2-225M-4 separator screen[17-18].

Table 1 Model parameters

| parameter | symbol | numerical value |
|---|---|---|
| vibrating screen mass/$kg$ | $m$ | 10000 |
| length of vibrating screen/$m$ | $2a$ | 6 |
| vibrating screen width/$m$ | $2b$ | 1.84 |
| $x-$ axis moment of inertia/$kg{\cdot}m^2$ | $J_x$ | 8710 |
| $y$-axis moment of inertia/$kg{\cdot}m^2$ | $J_y$ | 2460 |
| spring y direction stiffness/$N/m$ | $k_y$ | 1534000 |
| spring z direction stiffness/$N/m$ | $k_z$ | 4562000 |
| excited force/$N$ | $f$ | 260000 |
| excited frequency/$Hz$ | ω | 11 |
| gravitational capacity of silo/$N$ | $G$ | 400000 |
| The distance between the material storage and the center of mass/$m$ | $e$ | 3 |
| eccentric moment/$N{\cdot}m$ | $M_e$ | 5000 |
| Hourly processing capacity/$t$ | | 40 |

To facilitate the description and definition of spring damage

$$\Delta K_i=\frac{k_i-k_T}{k_i} \qquad (4)$$

In this formula, $\Delta K_i$ denotes the spring damage, $k_i$ represents the stiffness of spring i and $k_T$ indicates the actual stiffness of the spring.

## 4. Results

### 4.1 Amplitude of the Spleen Surface under Double Spring Damage

The amplitude of equation (4) under no-load conditions with different spring damage levels is plotted using the formula $New-Mark$β, as shown in Figures 3-6. In Figure 3, the y-direction amplitude of the dual springs (a), (b), and (c) shows that when $k_1/k_2$ is damaged, the gradient value ranges from 3 to 6. When $k_1/k_3$ and $k_1/k_4$ are damaged, the gradient values remain within 4-5, as illustrated by contour plots in Figures 3(a), (b), and (c). This indicates that the screen surface amplitude is more significantly affected by $k_1/k_2$ than by $k_3$ and $k_4$. At a damage level of 0.4, the amplitude of $k_1/k_2$ damage is slightly greater than that of other damage scenarios.

As shown in Figures 4(a), (b), and (c), gradient variations of 1 to 3 occur when $k_1/k_2$、$k_1/k_3$, and $k_1/k_4$ are damaged along the z-axis. The more they approach 0.4, the steeper the gradient changes, with $k_1/k_3$ showing the most pronounced effect. At a damage level of 0.4, the gradient value reaches 3.

As shown in Figures 5(a), (b), and (c), when $k_1/k_2$ is damaged, the amplitude varies linearly between 0.07 and 0.43. The gradient value ranges from 0.4 to 0.6. For $k_1/k_3$ and $k_1/k_4$ damage, the amplitude decreases as the damage level approaches zero, reaching zero when the damage is equal.

The amplitude fluctuates between 0 and 0.14, exhibiting a nonlinear relationship with spring damage. Both the amplitude variation and amplitude values are comparable and lower than those observed in$k_1/k_2$ damage, indicating that $k_1/k_2$ has a more significant effect on the amplitude in the θ direction.

As shown in Figures 6(a), (b), and (c), the amplitude values exhibit linear variations in the range of 0.24 to 1.6 when the$k_1/k_4$ spring is damaged. For $k_1/k_3$ and $k_1/$ springs, the amplitude range narrows to 0–0.52, with smaller values as the damage degree increases. When the damage degrees are equal, the amplitude drops to zero. The amplitude variation shows nonlinear dependence on spring damage degree. Both the amplitude change and magnitude are substantially smaller than those observed in$k_1/k_4$ cases, indicating that $k_1/k_2$ exerts a significant influence on the θ-direction amplitude.

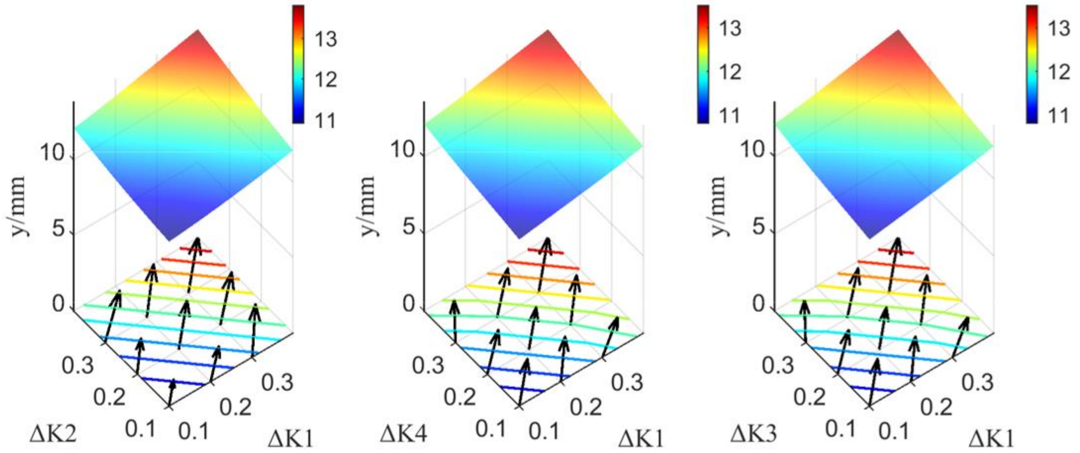

(a) Spring 1 and Spring 2 damaged (b) Spring 1 and Spring 4 damaged (c) Spring 1 and Spring 3 damaged

Fig.3 Double spring damage y amplitude

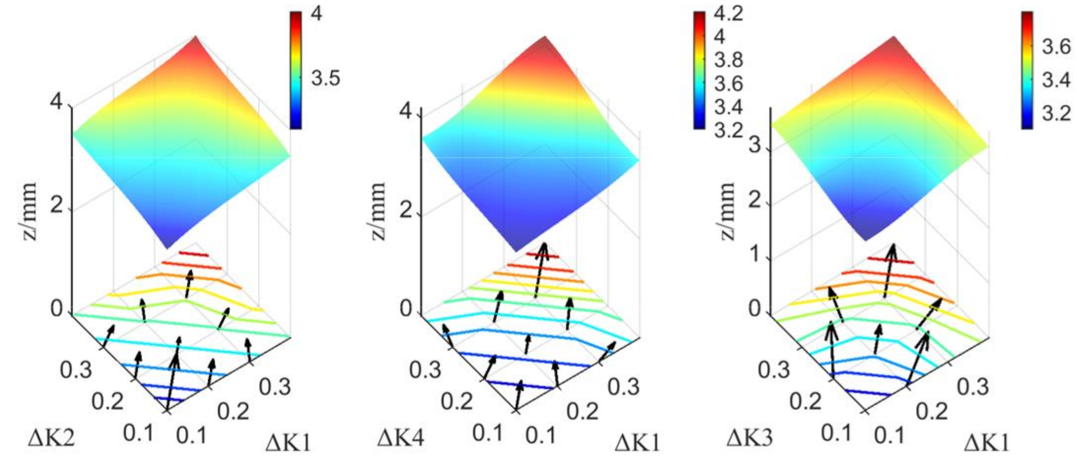

(a)Spring 1 and Spring 2 damaged (b) Spring 1 and Spring 4 damaged (c) Spring 1 and Spring 3 damaged

Fig4. Z-direction amplitude of double spring damage

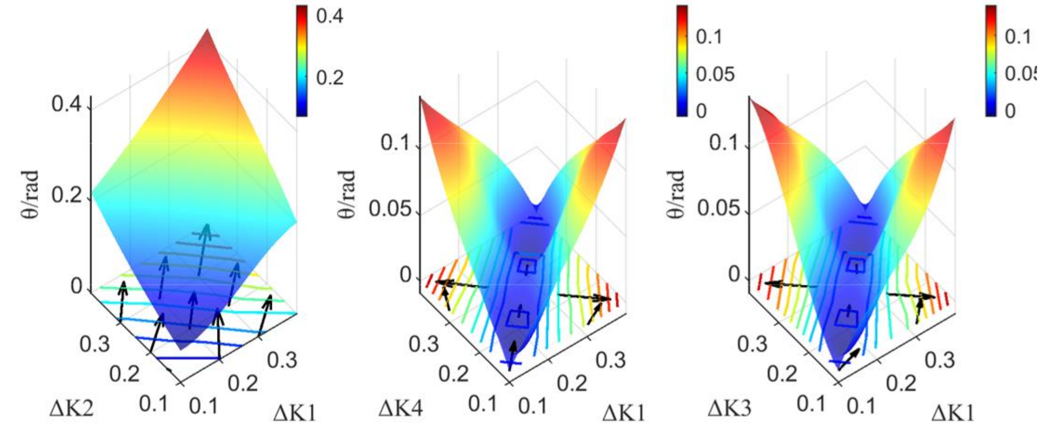

(a)Spring 1 and Spring 2 damaged (b) Spring 1 and Spring 4 damaged (c) Spring 1 and Spring 3 damaged

Fig.5 Double spring damage θ amplitude

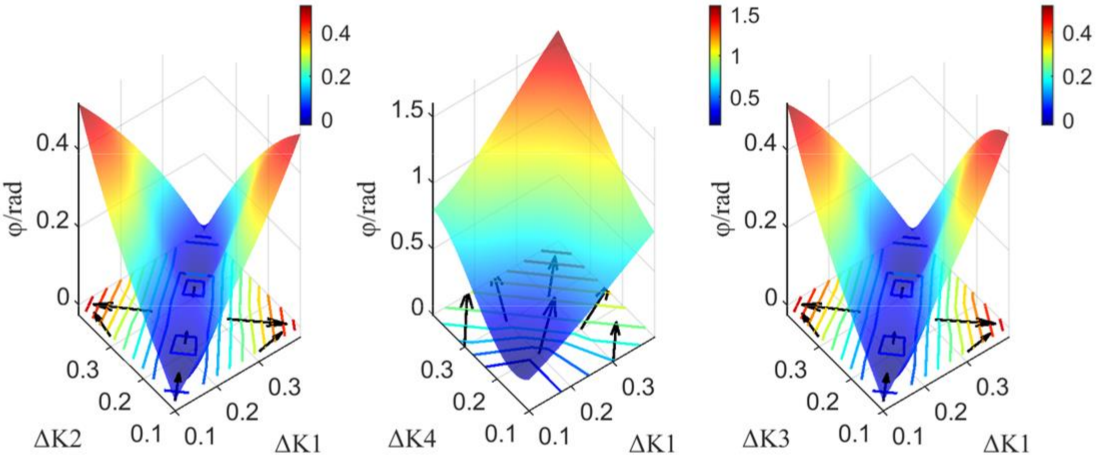

(a)Spring 1 and Spring 2 damaged (b) Spring 1 and Spring 4 damaged (c) Spring 1 and Spring 3 damaged

Fig.6 Double spring damage φ amplitude

## 4.2 Damage of the Double-position Spring and the Difference of Spring Displacement under Different Loads

The calculation of spring displacement is given in Equation 5. Utilizing the parameters listed in Table 1, the displacement differences under different load conditions and spring damage levels were calculated, and the results are presented in Figures 7–11. As depicted in Figures 7(a), 8(a), 9(a), and 11(a), when springs on the same side are damaged, the displacement difference between Spring 1 and Spring 2 exhibits a linear variation with the spring damage level, maintaining a consistent range of approximately 5 mm. In the case of diagonal spring damage, the displacement difference between Spring 1 and Spring 2 increases significantly, reaching a maximum of 6 mm.

Figures 7(b)–9(b) show that the same-side spring displacement difference increases with increasing load: at 10 tons, 40 tons combined with 0.5 tons of single-side loading, and 60 tons, the displacement differences range from 39 to 47 mm, 53 to 66 mm, and 78 to 93 mm, respectively. As indicated in Figures 9(b)–11(b), the location of spring damage has a negligible effect on the same-side displacement difference, which remains within the range of 51 to 56 mm. However, single-side loading applied to the screen surface increases the inter-spring displacement difference to 53 to 66 mm.

Figures 9(c)–11(c) illustrate that the displacement difference between Spring 1 and Spring 3 exhibits a linear correlation with their stiffness. Additionally, the inter-spring displacement difference shows a distinct dependence on the spring damage level: the minimum value is observed at a damage level of 0.1, while the maximum occurs at a damage level of 0.4. This indicates that a higher damage level leads to a larger displacement difference, whereas the load exerts a significant influence on the inter-spring displacement difference.

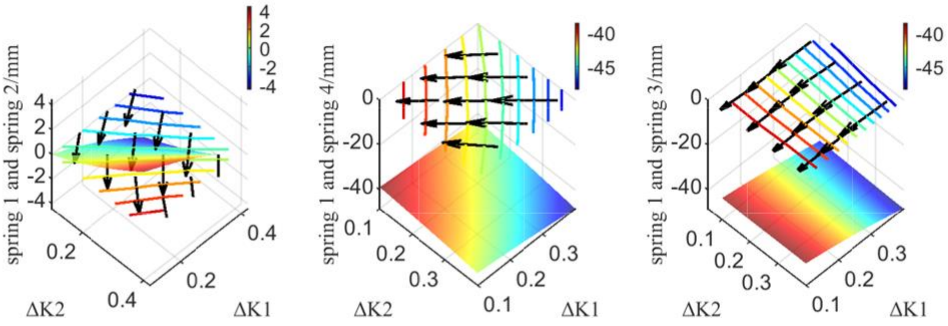

(a) (b) (c)

Fig.7 Spring displacement difference at each position of the 10-ton material warehouse load (k1/k2)

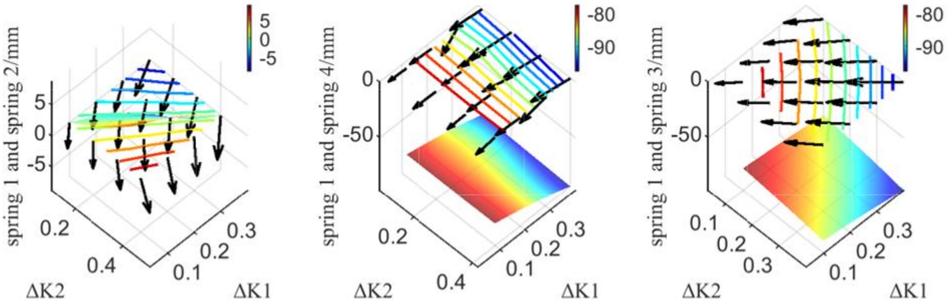

(a) (b) (c)

Fig.8 Spring displacement at each position when the load of the material warehouse is 60 tons

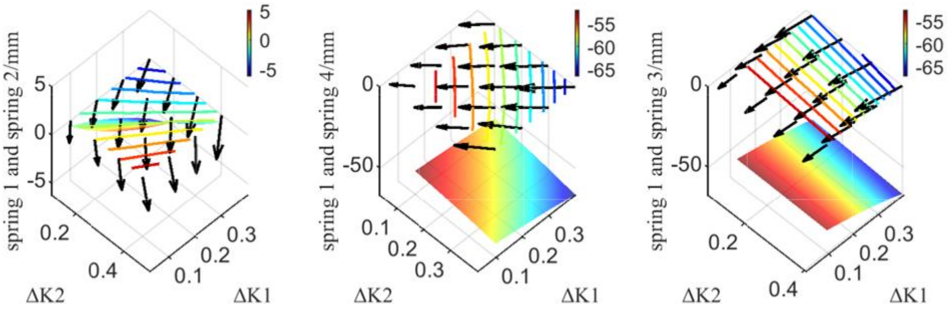

(a) (b) (c)

Fig.9 Spring displacement of 40 tons of material in the warehouse and 0.5 tons of single side stacking

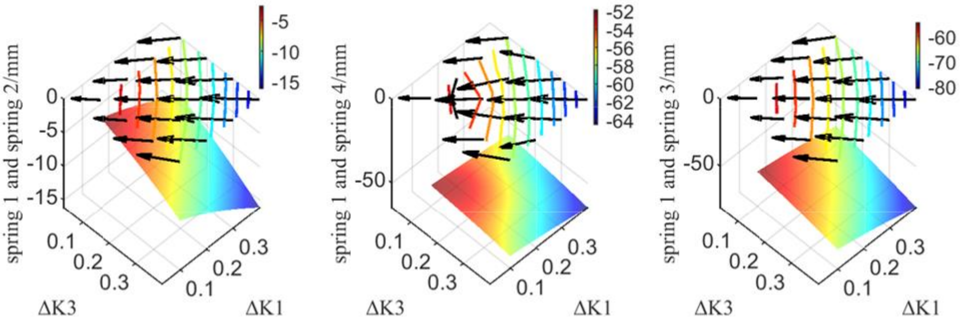

(a) (b) (c)

Fig.10 Damage of 40 tons of material $k_1/k_3$ in the storage

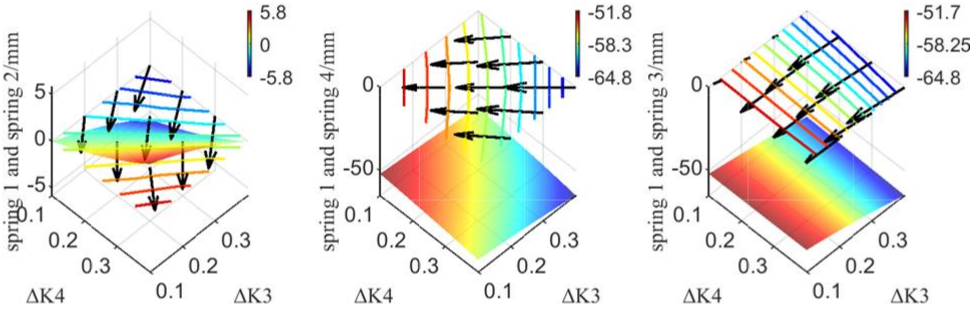

(a) (b) (c)

Fig.11 Damage to 40-ton $k_3/k_4$ storage silos

In conclusion, when the feed end of the vibrating screen is subjected to hopper loading, aggravated spring damage will increase the vibration amplitude of the screen surface. The stable negative displacement difference between the feed end and the discharge end confirms the occurrence of screen plane warping: specifically, the screen surface at the feed end sinks, while that at the discharge end arches upward.

Under the action of hopper loading, the feed-end screen surface undergoes initial displacement. Spring stiffness damage further enlarges the displacement difference between adjacent springs, which can reach approximately 10 mm, thereby exacerbating warping at both ends. When the hopper loading exceeds its critical value, the internal resistance of the material will surpass the excitation force, leading to a lower feed rate, material accumulation, and even the interruption of screening operations.

To avoid feeding difficulties caused by excessive spring displacement, it is essential to enhance the spring stiffness at the feed end.

## 5. Conclusions

(1) The Lagrange equation was employed to establish the dynamic model of the bar screen. During the modeling process, full consideration was given to the swinging torque induced by the uneven material distribution and the swinging torque caused by the silo load, leading to the construction of a dynamic equation for the four-degree-of-freedom bar screen.

(2) Analysis of the effect of spring damage on screen surface amplitude reveals that the amplitudes in both y and z directions increase linearly with the degree of spring damage at various positions, with the variation in these two directions remaining within 10%. In contrast, the amplitudes in θ and φ directions undergo more pronounced fluctuations (ranging from 20% to 100%), which are dependent on the location of the damaged spring and exhibit significant differences across different damage positions.

(3) The spring displacement difference of the separator screen is associated with the position of the damaged spring and the load condition. When the silo load is 60 tons, the maximum spring displacement difference can reach 93mm; a linear relationship exists between the spring displacement difference and the degree of spring damage.

(4) Under the silo load, the displacement difference between the feeding-end and discharge-end screen surfaces of the partition screen increases, accompanied by a reduction in the relative height of the two ends. This impairs the relative movement of materials and may result in feeding difficulties. Therefore, to ensure the stable operation of the partition screen, the spring stiffness at the feeding end should be enhanced, and damaged springs should be replaced promptly.

## References

*[1] Fang, P., Yang, Q., Hou, Y., et al. (2014). Theoretical study on self-synchronization of two homodromy rotors coupled with a pendulum rod in a far-resonant vibration system. Journal of Vibroengineering, 16(5), 2188-2204.*

*[2] Xia, X., Jing, W., Zhang, Z., et al. (2020). Simulation research, application status and development trend of vibrating screen. Journal of Central South University (Science and Technology), 51(10), 2689-2706.*

*[3] Fan, G., Liu, et al. (2024). Research on dynamic characteristics of complete dynamic model of vibrating screen based on spatial six degrees of freedom. Journal of China University of Mining and Technology, 53(1), 176-185. https://doi.org/10.1139/tcsme-2018-0134*

*[4] Gong, S., Wang, X., Yu, C., et al. (2019). Dynamic analysis of vibrating flip-flow screen based on a nonlinear model of shear spring. Journal of China Coal Society, 44(10), 3241-3249. https://doi.org/10.1016/j.powtec.2023.118312*

*[5] Liu, D., Peng, L., Wang, H., et al. (2020). Dynamic modeling and analysis of vibrating screen for vibration isolation of air spring with auxiliary chamber. Journal of the China Coal Society, 45(5), 1901-1908. https://doi.org/10.29202/nvngu/2019-1/6*

*[6] Harzanagh, A. A., Orhan, E. C., & Ergun, S. L. (2018). Discrete element modelling of vibrating screens. Minerals Engineering, 121, 107-121. https://doi.org/10.1016/j.mineng.2011.01.004*

*[7] Jiang, H., Yu, S., Zhao, Y., et al. (2021). Kinematics of rigid-flexible coupled high elastic screen surface and screening distribution law of material. Journal of China University of Mining & Technology, 50(5), 923-932. https://doi.org/info:doi/10.1166/asl.2011.1447*

*[8] Adenuga, O. T., Mpofu, K., & Ramatsetse, B. I. (2020). Exploring energy efficiency prediction method for Industry 4.0: a reconfigurable vibrating screen case study. Procedia Manufacturing, 51, 243-250. https://doi.org/10.1016/j.promfg.2020.10.035*

*[9] Bhattacharyya, S., Ghosh, A. D., & Basu, B. (2017). Nonlinear modeling and validation of air spring effects in a sealed tuned liquid column damper for structural control. Journal of Sound and Vibration, 410, 269-286. https://doi.org/10.1016/j.jsv.2017.07.046*

*[10] Ogunmodimu S O O ,Mainza N A ,Govender I , et al. Granular flow dynamics on vibrating screens: A mechanistic study[J].Minerals Engineering,2025,228, 109337. https://doi:10.1016/J.MINENG.2025.109337.*

*[11] Li L ,Xing Z ,Bai X , et al. String vibration model for FFVS's flexible screen and experimental study on high vibration intensity[J].Minerals Engineering,2025,228, 109319. https://doi:10.1016/J.MINENG.2025.109319.*

*[12] Barbosa M Y R ,Barbosa P V ,Waldmann A D T A , et al. VibraMap: A real-time tool for 3D Motion Characterization of shale shakers in production engineering applications[J].Production Engineering,2026,20(1):39:39. https://DOI:10.1007/S11740-025-01415-1*

*[13] Wu B ,Cao S ,Luo Q. Dynamic Characteristics of Vibrating Flip-Flow Screens Considering Material Impact Force[J].International Journal of Mechanical System Dynamics,2025,5(3):518-534. https:/doi/:10.1002/MSD2.70010.*

*[14] Wang, Z., Peng, L., Zhang, C., et al. (2019). Research on impact characteristics of screening coals on vibrating screen based on discrete-finite element method. Energy Sources, Part A: Recovery, Utilization, and Environmental Effects, 1-14. https://doi.org/10.1080/15567036.2019.1604905*

*[15] Moncada, M., & Rodr ǵuez, C. G. (2018). Dynamic modeling of a vibrating screen considering the ore inertia and force of the ore over the screen calculated with discrete element method. Shock and Vibration, 1-13. https://doi.org/10.1155/2018/1714738*

*[16] Zhang Z ,Wan H ,Wang L , et al. Collaborative optimization of screening efficiency and screen surface load in electromagnetic linear vibrating screen under variable frequency and amplitude[J].Powder Technology,2026,471122066:122066. https://DOI:10.1016/J.POWTEC.2025.122066*

*[17] ZHAI Hongxin. Determination of the operation range for flip-flow screen in industrial scale based on amplitude-frequency response [J]. Journal of China Coal Society, 2007, 32(7) : 753 －756. https://doi.org/10.1016/S1872-2067(07)60020-5*

*[18] ZOU Mengqi, LIU Chusheng, WU Jiada, et al. Influence of tensional amount on dynamic parameters of unilateral driven flip-flow screen surface[J]. Journal of China Coal Society, 2018,43(2)571 —567.*